

A Novel Low-Cost Channel Sounder for Double-Directionally Resolved Measurements in the MmWave band

Hussein Hammoud, Yuning Zhang, Zihang Cheng, Seun Sangodoyin,
Hofer Markus, Faruk Pasic, Thomas M. Pohl, Radek Závorka, Ales Prokes,
Thomas Zemen, *Senior Member, IEEE*, Christoph Mecklenbräuker, *Senior Member, IEEE*,
Andreas F. Molisch, *Fellow, IEEE*

Abstract—Since the design of wireless MIMO systems requires knowledge of the double-directional (i.e., directionally resolved at both link ends) channel characteristics, and 5G/6G use higher frequency bands, there is the need for double-directional measurements in the mmWave spectrum, along with channel sounders that can accurately perform such measurements. This paper introduces a novel channel sounding approach based on a redirecting rotating mirror arrangement (ReRoMA). The method is low-cost and flexible as it requires only a single radio frequency chain at each link end and performs mechanical beam-steering. However, in contrast to existing rotating-horn systems, it physically separates the signal generation/transmission and the beam steering components, resulting in orders-of-magnitude faster measurements. The paper outlines the fundamental concept, describes details of the implementation, and demonstrates its application and accuracy using a 60 GHz prototype for measurements in static reference scenarios, as well as dynamic measurements. We illustrate the detected propagation paths using dynamic angular and delay power spectra and correlate these findings with the surrounding environmental structure. Locations of environmental objects are detected within the Fourier resolution determined by bandwidth and horn width, with no noticeable degradation due to the faster measurements.

Index Terms—channel measurements, double-directional, channel modelling, mmwave, dynamic channels, v2v

I. INTRODUCTION

Motivated by the need for ever-increasing data rates and number of users, there is an ongoing trend in the wireless industry to exploit higher frequency bands, due to the large amount of fallow spectrum available in these bands. This trend results, e.g., in the use of mmWave bands for 5G deployment and the anticipated use of (sub)THz bands in 6G. Hence, both industry and academic researchers have shown a heightened

interest in systems operating within these frequency ranges. It is axiomatic that wireless communication system development requires a deep understanding of, and models for, the wireless propagation channel characteristics in the band of operation. Consequently, extensive and accurate channel measurements at high frequencies are critical for the effective development and testing of any robust and efficient system for communication, localization, sensing, or combinations thereof, in 5G/6G.

At higher frequencies, there is an inherent increase in the isotropic pathloss, making essential the use of adaptive arrays to improve the signal-to-noise ratio (SNR) [2, Chapter 4]. Furthermore, antenna arrays can also be used for the implementation of single-user multiple-input multiple-output (SU-MIMO) or multi-user MIMO (MU-MIMO) schemes to directly increase the throughput. For all these aspects, we need the *double-directional* channel characteristics, i.e., models and measurements need to be performed directionally resolved at both link ends.

Directional channel measurements require the use of multiple antennas, which can either be offset from each other in space (translational arrays), or can consist of directional antennas pointing into different directions (rotational arrays). In either case, the arrays can be real, switched, or virtual [2, Chapter 9]. In particular, virtual arrays using mechanically rotating horn antennas have been widely used in measurement campaigns over the past decade. Their main drawback is that the mechanical movement severely limits the measurement speed, which in turn limits both the number of points that can be measured in a campaign, and the scenarios that can be measured. Despite this, they remain a valuable and popular tool for detailed directional channel analysis (see Sec. I-A for a detailed literature survey of both this and alternative techniques).

The goal of the current paper is to overcome, or at least greatly mitigate, the limitations of mechanically-rotated horn arrays while retaining their advantages; in other words, to develop a flexible, cost-effective double-directional channel sounder that can perform *dynamic* channel measurements and measure order-of-magnitude more points per hour than a traditional rotated-horn setup. We achieve this goal by an approach we call ReRoMA (redirecting rotating mirror arrangement) [3]. It is based on the principle of separating the signal generation and transmission via a single fixed antenna,

H. Hammoud, Y. Zhang, Z. Cheng, and A. F. Molisch are with the Ming Hsieh Department of Electrical and Computer Engineering, University of Southern California. S. Sangodoyin is with the Georgia Tech's School of Electrical Engineering and Computer Engineering. H. Markus and T. Zemen are with the AIT Austrian Institute of Technology GmbH. F. Pasic, T. Pohl, and C. Mecklenbräuker are with the Institute of Telecommunications, Technische Universität Wien. R. Závorka and A. Prokes is with the Department of Radio Electronics at Brno University of Technology. The work of HH, YZ, ZC, and AFM was partly funded by a grant from CALTRANS in the METRANS program. The work of HM and TZ was funded within the Principal Scientist grant Dependable Wireless 6G Communication Systems (DEDICATE 6G). The work of RZ and AP was supported by the Czech Science Foundation under Lead Agency Project No. 23-04304L. Part of this work was submitted to IEEE ICC 2024 [1].

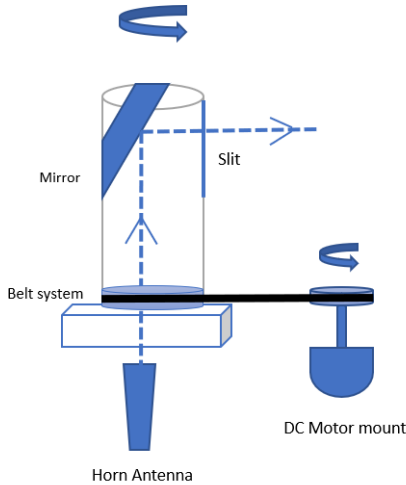


Fig. 1. ReRoMA sample configuration diagram

from a mechanically moving part that redirects the resulting beam. As depicted in Fig. 1, components like the horn antenna and cables remain stationary (no rotation), pointing upwards. The transmitted electromagnetic (EM) waves are redirected by a mirror inclined at an angle α , with $\alpha = 45^\circ$ enabling the beam to sweep across the horizontal plane. This mirror is placed inside a swiftly rotating tube, which changes the beam direction over time. As none of the rotating tube's components are connected to any electronic components, rotation can be *much* faster than in traditional sounders where the horn itself, and the cable attached to it, are rotated, see Sec. II-A for more details. As a matter of fact, a full "MIMO snapshot", i.e., a combination of all transmit and receive directions, can be obtained in about 1 s, compared to tens of minutes with traditional rotating horns.

A. State of the Art

So far, mmWave propagation has been investigated in different scenarios using several different types of channel sounders. The simplest channel sounders typically use single omnidirectional antennas on both the transmitter and receiver end such as the work in [4], [5]. These channel sounders are helpful in gathering pathloss, shadowing and delay-spread information. However, they lack directional information, and the large isotropic pathloss at mmWave frequencies can result in poor SNR. The latter problem may be overcome by using directional antennas (with fixed orientation) at one [6]–[8] or both [9] link ends, but this adds the problem of not detecting MPCs that fall outside the beamwidth of the used antennas, and still does not provide directional information.

For directional sounding, antenna arrays are required. Real arrays use multiple radio frequency (RF) chains to excite/capture multiple array elements simultaneously. While this allows the fastest measurements, such arrays are costly, difficult to implement and calibrate, and for mmWave systems are thus typically limited to small numbers of array elements [10]. Switched arrays also use multiple physical array elements but only a single RF chain, which is sequentially connected to

the different antenna elements via an electronic switch; though at higher frequencies the availability, power limitations, and attenuation of the switches can become challenging. Since electronic switches are fast, measurement of all combinations of transmit and receive elements (called a "MIMO snapshot") can be done on the order of a few, or a few tens, of milliseconds, depending on the array sizes. Examples for switched sounders at mmWave frequencies include [11], [12]. Improvements of the SNR can be achieved by switching between horn antennas, as realized in [13]. Ref. [14] presents a hybrid switched/real sounder.

Phased arrays switch beams sequentially into different directions and can generally achieve higher transmit power than switched arrays. A number of channel sounders based on this principle have been presented over the past years [15]–[21]. Typical number of antenna elements at each link end are between 8 and 256. Measurement times of a MIMO snapshot are similar to the switched-array case. Main challenges are availability and/or cost of phased arrays, in particular in newly-explored frequency bands.

Virtual arrays, such as those created by mechanically moving antenna elements across different preset location, measure different locations at different times. They are often combined with vector network analyzers (VNAs) to scan over frequency [22]–[24], but can also be combined with time-domain sounding [25]. Related to this are mechanically-steerable rotational arrays, created, e.g., by rotating horn antennas with stepper motors, sampling the channel from different angles. They can be combined with VNAs to scan over frequency for each horn orientation [26]–[28], transmission of pseudonoise sequences that are received with a correlation receiver [29]–[34], or multitone sounding [35], [36]. Such sounders have been used for measurements at a variety of frequencies in the mmWave band, e.g., 28 GHz [27], [29], [32], [33], 60 GHz [26], [35], 73 GHz [37] and at higher frequencies [30], [38]–[40], as well as multi-band [28], [34], [41]. They have been used for measurements in a wide variety of environments, ranging from indoor residential [42], indoor office [27], [33], [35], [41], shopping malls [28], [32], to outdoor device-to-device scenarios [39], [43], microcells [29], [30], [38] and even macrocells [44], [45]. Rotating horn sounders are significantly less expensive and easier to calibrate than full or phased arrays, and are useful in particular when investigating new frequency bands where phased arrays might not be available.

A key challenge is that these channel sounders are slow, due to the necessary mechanical movement, typically involving a stepper motor, when transitioning between different antenna positions. Moreover, the mechanical influences on cabling, such as cable twisting during horn rotation, can adversely affect the performance of high-frequency hardware. Although rotary joints can address this issue, their implementation comes with a substantial cost, particularly beyond 40 GHz, and they are prone to failure during prolonged operation [46]. While placing the entire sounder on a rotating platform resolves cabling concerns, it only allows for relatively slow rotation speeds (maximum 300 RPM) and has been implemented solely for narrowband sounding at 28 and 60 GHz [45], [47].

A system somewhat closer in spirit to the current paper was

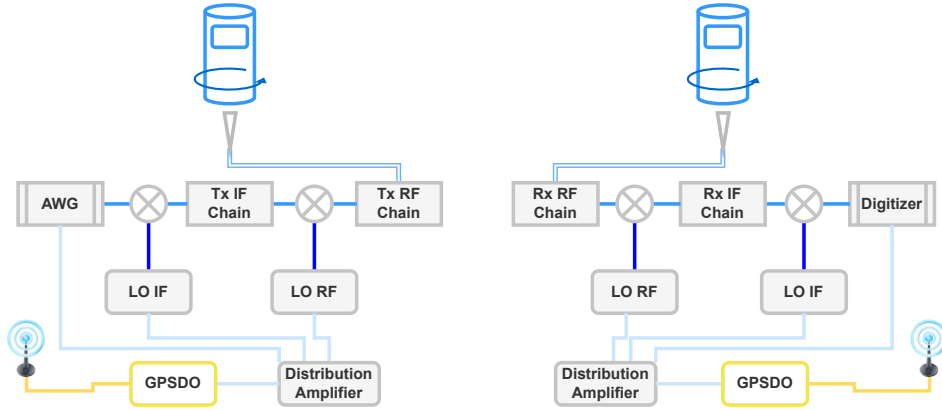


Fig. 2. High-level Sounder Diagram

presented by some of us in [48] where a rotating hemispherical shell, with an aperture cut into it, was placed over an omnidirectional antenna feed. This rotation allows mechanical beam steering but was only designed for beamforming at one link end, and rotation is slow and not appropriate for dynamic measurements (full rotation on one link end took several seconds). Furthermore, the fundamental operating principle was different, as in this approach the beam was *formed* by a rotating entity, while in the current paper an already-formed beam is *redirected* by the rotating entity.

B. Contributions

This paper’s primary scientific contributions are as follows:

- We present a novel approach to channel sounding utilizing the ReRoMA concept. This method strikes a unique balance between measurement speed, cost/complexity, and the requirement for specialized components. Notably, it maintains the simplicity of traditional rotating-horn sounders while enhancing measurement speed by at least two orders of magnitude.
- We detail the design, components, and calibration essential for the functioning of ReRoMA and introduce a functioning prototype demonstrating its capabilities.
- Utilizing this prototype, which operates at 60 GHz, we conduct double-directional reference and calibration measurements using a metallic sphere reflector and demonstrate the accuracy of the sounder. Additionally, we perform measurements in a dynamic measurement scenario (moving receiver (Rx)).

C. Organization of the paper

The remainder of the paper is organized as follows: Sec. II describes the principle and implementation details of the sounder, both in terms of mechanical and electronic components. Calibration is described in Sec. III, followed by the signal processing methods for the measurement evaluations in Sec. IV. Sec. V provides the results from sample measurement campaigns. Conclusions in Sec. VI wrap up the paper.

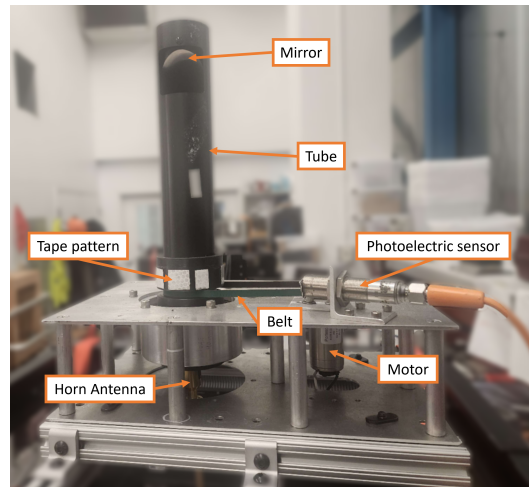


Fig. 3. ReRoMA Implementation in Hardware

II. SOUNDER SETUP

A. ReRoMa

1) *Mechanical Structure*: Our system’s mechanical structure at the transmitter (Tx)¹ contains two principal components: (i) *a fixed object (FO)*: this encompasses all the necessary electronics for generating the sounding signal, which is then transmitted upward through a horn antenna, which is also part of the FO, as depicted in Fig. 1. (ii) *a moving object (MO)* which redirects the waves emanating from the horn into time-varying directions, thus enabling the sounder to autonomously perform a comprehensive scan of the entire 360° azimuth plane. The MO consists of a cylindrical tube that is rotated by a belt drive powered by a direct current (DC) motor, see Fig. 3. The choice of this mechanism was guided by its ability to provide rotation that is both consistent (essential for accuracy and resolution) and fast (much faster than manual or stepper-motor methods).

A mirror set at an angle in the tube reflects the electromagnetic (EM) waves propagating vertically upwards from the horn at the base of the tube. The waves are redirected into the horizontal plane and exit through a slit on the side of

¹the Rx is completely analogous

the tube. The azimuth angle of the reflection depends on the rotation angle of the tube and thus changes quickly with time. Although our current design uses reflection into the horizontal plane, the mirror's angle is adjustable and can be tailored to suit different measurement scenarios. For instance, aligning the mirror downwards might be more suitable for measuring channels between an elevated device (e.g., base station (BS)) and devices on the ground (e.g., user equipments (UEs)).

Remark: Precise alignment of the horn antenna relative to the rotating tube is crucial. The antenna beam should precisely illuminate the mirror's center, facilitating beam reflection through the tube slit while minimizing internal reflections and waveguiding effects, which might lead to beam broadening and sidelobes. To achieve this, we designed a metallic mount that securely positions the antenna element beneath the tube's base, featuring high-precision adjustment screws that allow fine-tuned alignment adjustments of the horn antenna based on calibration with a laser pointer.

2) *Rotation Speeds and Angular Resolution:* The mechanical rotation principle at the Rx and Tx requires a careful trade off between angular and temporal resolution for the intended identification of radio propagation mechanisms in (slowly) mobile scenarios in the mmWave band.

We can achieve a mechanically safe and stable rotation speed of $N_{\text{Rx}} = 2080 \text{ rpm} = 34.67 \text{ Hz}$ with our prototype where rpm indicated rotations-per-minute. Hence, a complete Rx rotation takes $T_{\text{Rx}} = 1/N_{\text{Rx}} = 28.8 \text{ ms}$.

We aim at sampling close to critical with respect to the antennas angular beam width. Hence, we chose a temporal sampling time of $T_s = 200 \mu\text{s}$, with measurements of the two polarizations interlaced as is explained in II-A4. Thus, the effective sampling time for each polarization is $2T_s$, and we obtain $M_{\text{Rx}} = 1/(2N_{\text{Rx}}T_s) = 72$ angular impulse response measurements per revolution at the Rx side, spaced $\Delta\beta_{\text{Rx}} = 360/M_{\text{Rx}} = 5^\circ$. Hence, for our Rx beamwidth of $\beta_{\text{Rx}} = 9^\circ$ we achieve a normalized sampling rate of $\Delta\beta_{\text{Rx}}/\beta_{\text{Rx}} = 0.55$.

The Tx performs a slower stable² rotation at a speed of $N_{\text{Tx}} = 57.8 \text{ rpm} = 0.963 \text{ Hz}$. Hence a complete rotation takes $T_{\text{Tx}} = 1/N_{\text{Tx}} = 1.038 \text{ s}$. The number of measured angular positions on the Tx side per Tx revolution is thus $M_{\text{Tx}} = N_{\text{Tx}}/N_{\text{Rx}} = 36$ spaced at $\Delta\beta_{\text{Tx}} = 360/M_{\text{Tx}} = 10^\circ$. To adhere to the principle of capturing more than one sample per 3 dB beamwidth, a different horn antenna is used for the Tx, with a 3 dB beamwidth of $\beta_{\text{Tx}} = 25^\circ$, achieving a normalized sampling rate of $\Delta\beta_{\text{Tx}}/\beta_{\text{Tx}} = 0.4$. Worth to note however that sampling at 3 dB beamwidth is a minimum requirement; sampling at faster than 3 dB beamwidth would lead to a better parameter estimation accuracy and a higher SNR, as long as the hardware on the receiver side (digitization and data streaming) is able to support it. Rotating at such different speeds between the Tx and the Rx allows sampling the channel in an angular pattern similar to the stepper-motor-based sounders, where the Rx steps into all angular positions

²Proper calibration of the rotation speeds might be necessary especially at the Tx side because of possible instability at low speeds. Such calibration in addition to precise angular encoding (see next section) would alleviate this problem.

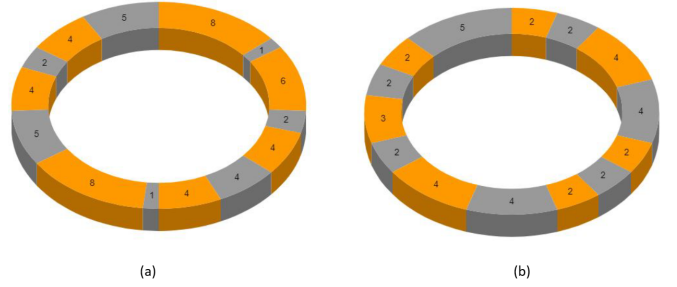


Fig. 4. Reflector tape pattern on (a) Rx and (b) Tx

for each Tx position³. This implies that the full MIMO snapshot capture time (i.e. the time during which all 36×72 combinations of Tx and Rx positions are measured) is 1.038 s. While this duration is shorter than the typical stationarity times of channels (the period during which channel statistics remain constant) envisioned for our measurement environment and speeds [49], it exceeds the coherence time (approximately the inverse of the Doppler spread) of most channels. This indicates that our sounder is not capable of measuring the Doppler spectrum.

3) *Angular Encoding and Mapping:* To achieve the high rotational speed, ReRoMA uses a "free-running" motor. Deviations from the nominal (intended) orientations are acceptable as long as they are measured and incorporated in the reconstruction of the double-directional impulse response. Hence, we measure the angular orientation $\alpha_{\text{Tx}}[m]$ and $\alpha_{\text{Rx}}[m]$ at the moment of signal capture $t = mT_s$ using an optical photoelectric sensor system, $m \in \mathbb{Z}^+$ indicated the discrete impulse response index. We use a polarized reflective tape affixed to the MO, with the sensor itself mounted atop the FO. The use of *polarized* tape ensures enhanced resistance to ambient light interference.

To achieve high precision we place multiple pieces of tape along the tube circumference, resulting in a distinct (coded) sequence of dark, non-reflective and light, reflective sections. The pattern is designed with the following two constraints: (i) Low auto-correlation of the pattern sequence except at zero-shift, thus allowing precise correlation between sensor readings and physical tube direction, and (ii) dark and light region width based on the sensor resolution, i.e. matching the width of the polarized light beam emitted by the photoelectric sensor. The patterns used in our prototype at Tx and Rx⁴ are shown in Fig. 4.

The sensor information is gathered using National Instruments (NI) DAQ boards, which operate at different sampling rates for the Tx and Rx due to their varying rotation speeds. The sampling times are $\theta_{\text{Tx}} = 8.3 \mu\text{s}$ and $\theta_{\text{Rx}} = 0.4 \mu\text{s}$. The optical sensor data is stored together with a GPS timestamp

³Note however that while they are similar, it is not exactly the same. In ReRoMA, neither the Tx nor the Rx "stops" in certain angular positions, they are always in continuous rotation. However, they can be assumed stationary during the capture duration (Tx and Rx rotate 0.005° and 0.4° during a digitizer capture respectively.)

⁴Note that the same tape pattern could have been used on both the Tx and the Rx. The difference in our design was only for convenience and distinction between Tx and Rx both in hardware and in processing codes.

to align the sensor orientation with the collected impulse response measurement during post processing.

4) *Polarization*: In principle any polarization of the Tx horn can be used in ReRoMA. Linear polarization is widely used for horn antennas and thus seem like a natural choice. However, in this case the polarization vector of the redirected wave alters its orientation angle depending on the position of the mirror: for example, if the E-vector of the wave emanating from the horn is along the x-axis, the vector of the reflected wave will be along the z-axis at 0 degree azimuth of the tube, but along the x-axis when the tube is at 90 degree azimuth. It is thus beneficial to employ circular polarization, because the redirected wave has the same handedness for all tube orientations.

At the same time, it is crucial to remember that circular polarization changes its handedness upon reflection. Thus, assuming the same circular polarization direction employed on both the Tx and Rx, we would only correctly capture multipath components (MPCs) that have undergone an even number of reflections. An MPC reflected an odd-number of times would be attenuated by the cross-polarization ratio at the Rx. Therefore, to fully characterize the channel, we must receive both types of circular polarization - left-handed circular polarization (LHCP) and right-handed circular polarization (RHCP) - at the Rx end. For this purpose, we switch between the two polarizations, measuring them *quasi*-simultaneously. Specifically, the switching happens every-other capture using a trigger signal with period of $200 \mu\text{s}$. While the switching between polarizations might be alternatively implemented also at the Tx, this would require polarization switches with higher power handling capabilities. Additionally, in order to be able to estimate the full polarimetric channel matrix, polarization switches would be needed on both Tx and Rx. Such system is envisioned in future extensions of this work.

In our prototype we have used the Mi-wave Series 145 polarization switch [50]. The switching of this device occurs in a ferrite section which is made up of a Faraday rotator. It consists of a small circular ferrite rod which is supported by a Teflon cylinder in a thin-walled stainless steel waveguide. A coil wound around this waveguide provides the magnetic excitation in the ferrite where different excitation current values rotate the incident electric field by different angles. The excitation currents required for switching between LHCP and RHCP were carefully calibrated using a VNA, and the fast switching between current values was done by a current-mirror transistor circuit in combination with an op-amp to allow for the required current swing.

B. Electronic Components

This subsection discusses the creation and detection of the sounding signal. The fundamental design of our ReRoMA channel sounder is not dependent on the details of these processes - the sounding signal exciting the Tx horn can be generated in a large variety of ways. Instead, the forthcoming explanation is intended to provide a clearer understanding of the operational prototype's performance and the outcomes (including their limitations) obtained from its measurements. This

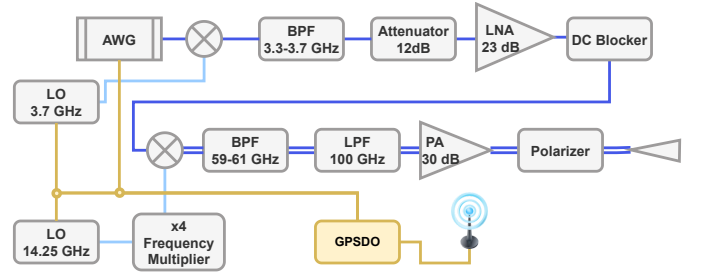


Fig. 5. Detailed Tx chain

helps in interpreting the measurement results and evaluating the sounder's effectiveness in various scenarios. A high-level schematic for our sounder can be seen in Fig. 2.

1) *Sounding Waveform*: For our sounding signal, we use multi-tone signals that resembles Zadoff-Chu sequences found in LTE and NR (new radio). Our sequences are designed to provide flat spectrum and low peak-to-average power ratio (PAPR) of signals even when they are filtered and over-sampled [51]. The sounding signal spans a bandwidth of $BW = 200 \text{ MHz}$, composed of $N_{sc} = 400$ subcarriers. This results in a subcarrier spacing of $\Delta f_{sc} = BW/N_{sc} = 500 \text{ kHz}$ which enables the clear identification of propagation distances up to a maximum of $D_{max} = c\tau_{max} = c/\Delta f_{sc} = 600\text{m}$ where c is the speed of light. We anticipate this range to be more than sufficient for all our measurement scenarios.

In terms of distance resolution, the 200 MHz bandwidth allows for a precision of $\Delta d = c\Delta\tau = c/BW = 1.5\text{m}$. Worth to note that While we currently use this 200 MHz bandwidth primarily as a proof of concept, the ReRoMA system itself would only impose a limit in the bandwidth of the horn antennas, enabling possibly tens of GHz if the signal generation electronics can provide that.

The sounding waveform is digitally shifted to passband. For the measurement, it is initially triggered by a 1 PPS (pulse per second) signal from a GPS-disciplined clock and then continues to repeat indefinitely. Each cycle of this waveform lasts for $T_{wf} = 2 \mu\text{s}$.

2) *Tx Chain*: The diagram of the Tx RF chain is shown in Fig. 5. The previously mentioned pre-loaded sounding waveform is output from the AWG and upconverted by an initial mixing stage to a first intermediate frequency (IF) with center frequency of 3.7 GHz where one of the sidebands is filtered before the signal is upconverted to the 60 GHz band, where a band-pass filter is used to confine the transmitted frequencies within the $59 - 61 \text{ GHz}$ band.

In the RF stage, a power amplifier boosts the signal power to 22 dBm , after which a polarizer forces the signal's polarization to LHCP. Finally, the signal is sent from the Tx antenna. For our experiments, we utilized a conical horn antenna with a beamwidth of 25° .

3) *Rx Chain*: The Rx RF chain's layout is depicted in Fig. 6. The signal transmitted through the wireless channel is received using a conical horn antenna with a beamwidth of 9° . The antenna output then enters a dual-function device that acts as both a polarization-switch and polarizer, capable of alternating between LHCP and RHCP. Following this, the

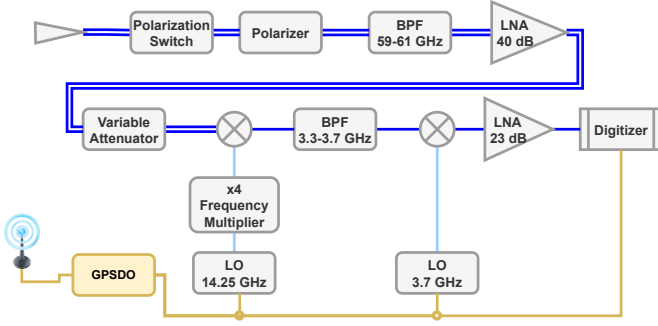


Fig. 6. Detailed Rx chain

signal passes through a cascade of a bandpass filter, a low-noise amplifier (LNA) and a variable attenuator that allows for the fine-tuning of the input power into the downconverter based on the specific measurement scenario.

The output of the attenuator is downconverted to 3.7 GHz IF where further filtering is applied. Subsequently, a second down-mixing process brings the center frequency to 300 MHz frequency. This step is followed by another amplification using a second LNA, which is tailored to match the voltage swing requirements of the digitizer. Finally, the processed signal is captured and stored by a National Instruments PXIe-5162 digitizer for later analysis and processing.

A summary of all sounder parameters is given in Table I.

Parameter	Symbol	Value
Frequency subcarriers	N_{sc}	400
Waveform duration	T_{wf}	$2 \mu s$
RF frequency range	$f_{start} - f_{end}$	60.3-60.5 GHz
Measured bandwidth	BW	200 MHz
Maximum bandwidth	BW_{max}	1 GHz
Tx Antenna 3dB Beamwidth	β_{Tx}	25°
Rx Antenna 3dB Beamwidth	β_{Rx}	9°
Tx/Rx rotation range	$[\phi_{start} : \phi_{end}]$	$[-180^\circ : 180^\circ]$
Tx rotation resolution	$\Delta\beta_{Tx}$	10°
Tx antenna positions	M_{Tx}	36
Rx rotation resolution	$\Delta\beta_{Rx}$	5°
Rx antenna positions	M_{Rx}	72
Capture trigger period	T_s	$200 \mu s$
SIMO snapshot duration	T_{SIMO}	28 ms
MIMO snapshot duration	T_{MIMO}	1.038 s
Dynamic range	DR	45 dB
Sampling rate	R_s	1.25 GSps

TABLE I
SOUNDER PARAMETERS

C. Synchronization

The timing for capturing the signal is synchronized using a GPS-disciplined 10 MHz and 1 PPS signals. Initially, the capture process is activated by the 1 PPS signal, enabling the

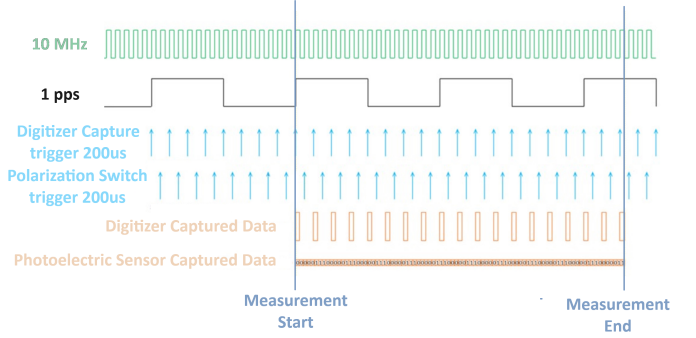


Fig. 7. Timing sequence and triggering

synchronization of the AWG's transmission and the digitizer's reception with the precision of the 1 PPS signal. Following this initial 1 PPS trigger, a subsequent trigger, derived from the 10 MHz signal, governs the sampling process, operating with a $200 \mu s$ period. This secondary trigger maintains accurate synchronization between the Tx and Rx. Additional clock drift experienced during the measurement campaign can be corrected for in post-processing by linear interpolation of the drift in between reference LOS calibration measurements.

The chosen trigger period is set to facilitate the capture of the received signal by the digitizer each time the receive direction rotates by half the beamwidth of the antenna. Since the sampling periodicity is considerably larger than the duration of the sounding signal, the deadtimes during reception can be used for streaming the sampled signal to an external recording devices. Such duty cycling would not be necessary when the backplane of the digitizer supports a data rate that is sufficient for continuous streaming.

To coordinate the switching of the polarization switch, another trigger signal is employed, featuring a $100 \mu s$ delay relative to the primary $200 \mu s$ trigger. This switching occurs during the digitizer's downtime. This method ensures that the polarization switch transitions are integrated into the capture cycle, avoiding any interference with the ongoing data acquisition. Fig. 7 illustrates the various triggers and their respective roles in the signal capture process is provided in.

III. CALIBRATION MEASUREMENTS

The back-to-back (B2B) calibration of our setup was done as follows: We first measure the over-the-waveguide ($H_{OTW|o}(f_k)$) system response by disconnecting the horn antennas from the setup in Fig. 2 and connecting the corresponding ports with a cascade of waveguides, where f_k is the frequency index. This allows to measure the full frequency response of our system in addition to these waveguide extensions. The frequency response of the waveguide extensions ($H_{Waveguides}(f_k)$) is then measured with a VNA. The B2B calibration response, per polarization direction o as chosen by the polarization switch at the Rx side, can therefore be calculated as

$$H_{B2B|o}(f_k) = \frac{H_{OTW|o}(f_k)}{H_{Waveguides}(f_k)} \quad (1)$$



Fig. 8. Google Earth view of measurement environment. Tx and Rx locations are marked in red and blue respectively.

We next calibrate the antenna characteristic, by performing pattern measurements, for the Tx and the Rx separately, in an anechoic chamber. The device-under-test (DUT) is rotated in azimuth in steps of 5° , while a reference horn antenna with known characteristic is used at the other link end. These measurements were performed twice, once with the DUT being the horn antenna alone, and once with the DUT being the whole (FO+MO) setup of one link end, to observe the pattern differences between those two situations. We note that the beampattern shape was the same for the two measurements, with a slightly more attenuation (~ 1 dB) caused by the mirror reflection. We use the latter pattern measurement, denoted as $b_T(\phi, f)$, $b_R(\phi, f)$ in our evaluation as outlined in Sec. IV.

In addition to the standard calibration procedures described above, and because of the difference of our sounding method compared to other sounders, we performed two additional verification measurements to verify (i) the stability of our sounder, and (ii) the comparability of our results to the traditional stepper-motor rotating horn sounders.

The first measurement evaluates the time and power stability of the sounder over a long duration. We measured a stationary environment for one hour, with a full MIMO snapshot captured every one second, using a single GPSDO (GPS disciplined oscillator) connecting to distribution amplifiers on the Tx and the Rx sides. The measurement was performed in the Epstein Family Plaza at USC. We show a satellite view of the environment in Fig. 8.⁵ A rough schematic for the environment was generated in MATLAB, see Fig. 9. This simplified geometry will be used for comparison with measurements in the remainder of the paper, as it accounts for the dominant propagation mechanisms in the channel.

To verify the stability of the sounder, we plot and overlap the noise-thresholded omnidirectional power-delay profiles (Omni-PDP), calculated by selecting the direction of the maximum power contribution per delay bin, of all of the MIMO snapshots captured within the one hour duration, and we show the results in Fig. 10. We clearly observe the highly

⁵This environment is used in subsequent measurements but with addition of objects acting as reflectors

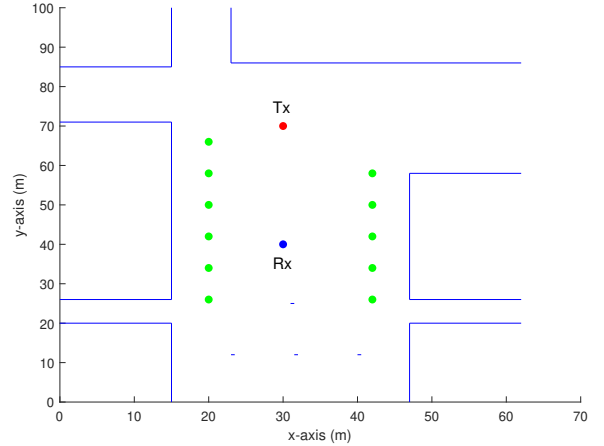


Fig. 9. MATLAB view of measurement environment. Surrounding trees (green) and building walls (blue). Red and blue dots corresponds to Tx and Rx locations respectively.

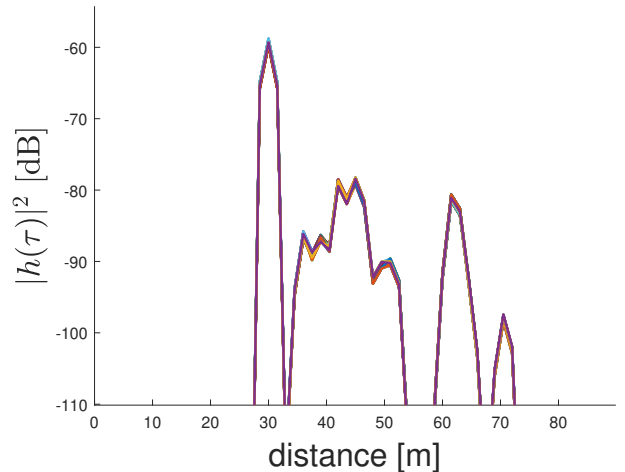


Fig. 10. Omni-PDP for the 1 hour measurement, overlapped

stable performance of the sounder where all of the APDPs are well overlapped. The main difference comes from APDP samples that are close to the noise-threshold, 30 dB or more below the peak amplitude.

The second measurement was to verify the angular stability as well as agreement with the well-established stepper-motor rotating horn approach. We thus measured the same scenario once with our fast-rotating motors sampling the full MIMO channel every one second, and a second time by manually stepping the angle of rotation of the tube to mimic a stepper motor approach. Due to the time and effort needed to perform the manual measurement, only 12 angular steps (one step every 30°) were measured at both Tx and Rx, thus creating a 12×12 MIMO snapshot. The measurement was done in the same location as the previous (long-term) measurement (see Fig 9).

To provide a fair comparison between the two different scenarios, we sub-sample the 72×36 MIMO snapshot captured by the motor rotation down to a 12×12 MIMO snapshot, i.e. taking every sixth angular step on the Rx, and every

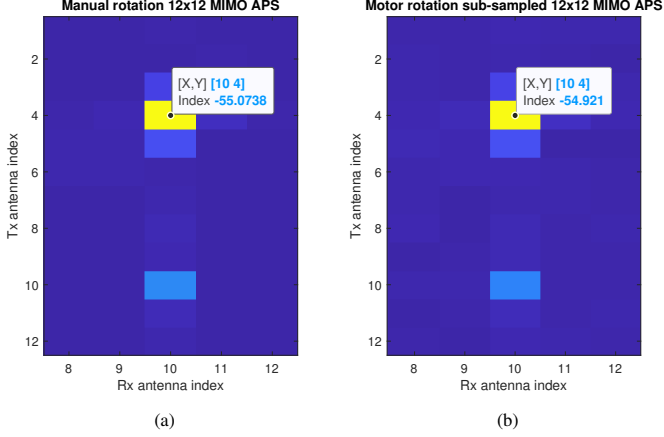


Fig. 11. APS comparison for the 12x12 MIMO snapshot generated by (a) Manual rotation, (b) Motor rotation with sub-sampling

third on the Tx. Fig. 11 shows the APS (angular power spectrum), calculated as the total power per Tx-Rx antenna pair, generated by the two scenarios; we only plot the angular range corresponding to five positions on the Rx side, namely the antenna directions where we actually see reflectors heavily contributing to the channel response. We calculate the RMSE between the two generated APSs and note a difference of less than 1 dB, confirming the equivalence between our sounding approach and the stepper-motor rotating horn approach.

IV. EVALUATIONS PROCEDURE

As outlined in the preceding sections, the objective of this work is to analyze and characterize the double-directional propagation channel between two link ends, measured from a Tx to an Rx, though channel reciprocity allows determination of the reverse direction as well. The dynamic, complex double-directional channel transfer function can be written as the sum of the contributions from N MPCs [52]:

$$\mathbf{H}(f, \varphi_{R,q}, \varphi_{T,p}) = \sum_{l=1}^N \alpha_l b_{\mathbf{T}}(\phi_{T,l} - \varphi_{T,p}, f) b_{\mathbf{R}}(\phi_{R,l} - \varphi_{R,q}, f) e^{-j2\pi f \tau_l} \quad (2)$$

where α_l , τ_l , $\phi_{T,l}$ and $\phi_{R,l}$ are the complex amplitude, propagation delay, direction-of-departure (DoD) and direction-of-arrival (DoA) of the l^{th} path, respectively, and $b_{\mathbf{T},p}(\varphi_{T,p}, f)$ and $b_{\mathbf{R},q}(\varphi_{R,q}, f)$ are the transmitter and receiver complex antenna gain pattern centered at the p^{th} and q^{th} orientation, where the horn points into $\varphi_{T,p}$, $\varphi_{R,q}$ respectively.⁶ These angles are time-dependent, but change on a scale that is much longer than the duration of the sounding signal $x_{\text{wav}}(t)$; for convenience of notation we henceforth do not explicitly write this time dependence. This model assumes that wave propagation occurs only in the horizontal plane, i.e., elevation is not considered.

The received signal at time t is the convolution of the sounding sequence with the channel impulse response and the

⁶Note that the calibration pattern is measured only once, and has its maximum in direction 0 for both Tx and Rx.

system (back-to-back) impulse response, which can also be written as

$$\begin{aligned} r_{\text{meas}}(t, \varphi_{R,q}, \varphi_{T,p}) &= \mathcal{F}_f^{-1} \{ \mathbf{R}_{\text{meas}}(f, \varphi_{R,q}, \varphi_{T,p}) \} \\ &= \mathcal{F}_f^{-1} \{ \mathbf{H}(f, \varphi_{R,q}, \varphi_{T,p}) \mathbf{H}_{\text{B2B}}(f) X_{\text{wav}}(f) \} \quad (3) \end{aligned}$$

where \mathcal{F}_f^{-1} is the inverse fast Fourier transform (IFFT) with respect to f , $\mathbf{H}_{\text{B2B}}(f)$ is the back-to-back transfer function of the system and $X_{\text{wav}}(f)$ is the sounding waveform.

For our measurement, considering all the factors mentioned earlier, and taking into account the datasets collected during the measurement campaign (which include timestamped ADC captures and timestamped Tx and Rx sensor data), the received signal \hat{r}_{meas} on a rectangular grid are approximated from the measured sample values r_{meas} as

$$\begin{aligned} \hat{r}_{\text{meas}}(nT_s, \hat{\varphi}_{R,q}, \hat{\varphi}_{T,p}) &= \mathcal{F}_f^{-1} \{ \hat{\mathbf{R}}_{\text{meas}}(f, \hat{\varphi}_{R,q}, \hat{\varphi}_{T,p}) \} \\ &\approx r_{\text{meas}}[nT_s, \varphi_{R,q}, \varphi_{T,p}] \quad (4) \end{aligned}$$

where T_s is the ADC trigger period set at $200\mu\text{s}$, and $(\hat{\varphi}_{R,q}, \hat{\varphi}_{T,p})$ are calculated by projecting the measured (Rx,Tx) angular orientation $(\omega_{\mathbf{R}}(nT_s), \omega_{\mathbf{T}}(nT_s))$ onto the nearest rectangular grid point $(\hat{\varphi}_{R,q}, \hat{\varphi}_{T,p})$, where this rectangular grid was created by taking the center points of the angular orientation between two consecutive temporal samples on both the Tx and the Rx. A more elaborate approach of interpolating the diagonal grid into a rectangular grid by means of non-uniform and sparse sampling is envisioned for future work. The resulting separation between grid points is 10° and 5° on the Tx and Rx side respectively. In this context, we operate under the assumption that the tubes on both the Tx and Rx sides remain stationary during the brief capture duration of $16\mu\text{s}$, corresponding to 8 repetitions (that are averaged) of the $2\mu\text{s}$ -duration waveform for a single Tx-Rx directional pair.

The measurement data for the two polarization directions can therefore be arranged in three-dimensional matrices whose entries are $\hat{\mathbf{R}}_{\text{meas}|\text{co}}(f_k, \hat{\varphi}_{R,q}, \hat{\varphi}_{T,p})$ and $\hat{\mathbf{R}}_{\text{meas}|\text{cross}}(f_k, \hat{\varphi}_{R,q}, \hat{\varphi}_{T,p})$, with the dimensions $N_f \times N_{\text{Rx}} \times N_{\text{Tx}}$ where f_k is the frequency index, $\hat{\varphi}_{R,q}, \hat{\varphi}_{T,p}$ are the rectangular antenna positions we have projected our angular data onto, N_f is the number of frequency points, and N_{Rx} and N_{Tx} are the total number of directions on Rx and Tx sides, respectively. We then eliminate the effects of the system transfer function (the transfer function of our sounder) and the antenna patterns for both the Tx and the Rx as described in the calibration section to eventually compute the calibrated directional channel transfer function \mathbf{H} as

$$\begin{aligned} \mathbf{H}(f_k, \hat{\varphi}_{R,q}, \hat{\varphi}_{T,p}) &= \\ &= \frac{\hat{\mathbf{R}}_{\text{meas}|\text{co}}(f_k, \hat{\varphi}_{R,q}, \hat{\varphi}_{T,p})}{\mathbf{H}_{\text{B2B}|\text{co}}(f_k) b_{\mathbf{T}}(0, f_k) b_{\mathbf{R}}(0, f_k)} + \\ &= \frac{\hat{\mathbf{R}}_{\text{meas}|\text{cross}}(f_k, \hat{\varphi}_{R,q}, \hat{\varphi}_{T,p})}{\mathbf{H}_{\text{B2B}|\text{cross}}(f_k) b_{\mathbf{T}}(0, f_k) b_{\mathbf{R}}(0, f_k)} \cdot \quad (5) \end{aligned}$$

From this, the directional power delay profile (PDP) is computed as

$$P_{\text{direc}}(\tau, \hat{\varphi}_{R,q}, \hat{\varphi}_{T,p}) = |\mathcal{F}_{f_k}^{-1}\{H(f_k, \hat{\varphi}_{R,q}, \hat{\varphi}_{T,p}) \cdot W_{\text{hann}}(f_k)\}|^2 \quad (6)$$

where $\mathcal{F}_{f_k}^{-1}$ is the inverse fast Fourier transform (IFFT) with respect to f_k , and W_{hann} is a Hann window applied in the frequency domain, which suppresses sidelobes in the delay domain at the expense of slightly broadening the main lobe of the impulse response. Finally, we apply noise thresholding and delay gating, similar to [39]:

$$P(\tau, \hat{\varphi}_{R,q}, \hat{\varphi}_{T,p}) = \begin{cases} P_{\text{direc}} & \text{if } (\tau \leq \tau_{\text{gate}}) \wedge (P_{\text{direc}} \geq P_{\lambda}) \\ 0 & \text{otherwise} \end{cases} \quad (7)$$

where τ_{gate} is the delay gating value selected to avoid incorporation of points with longer delay than what can be created in the considered environment, as well as points with “wrap-around” effect of the IFFT, and P_{λ} is the noise threshold. The thresholding eliminates noise-only delay bins, whose contributions would distort estimation of delay- and angular-dispersion parameters [53]. For our current measurements, τ_{gate} is set to 250 m excess runlength, while P_{λ} is selected to be 6 dB above the average noise power level of the PDP.

For analyzing the channel behavior from an “omni-directional” perspective, we synthesize the omni-PDPs by an approach similar to [32], i.e. by reconstructing the omni-directional pattern from the full double-directional capture by selecting the maximum power component (the direction of the highest contribution) per delay bin

$$P_{\text{omni}}(\tau) = \max_{\hat{\varphi}_{R,q}, \hat{\varphi}_{T,p}} P(\tau, \hat{\varphi}_{R,q}, \hat{\varphi}_{T,p}) \quad (8)$$

In addition, to analyze the channel behavior from an angular perspective, we generate the angular and delay power spectrum (ADPS) at both the Tx and the Rx as

$$\text{ADPS}_{\text{Tx}}(\tau, \hat{\varphi}_{T,p}) = \sum_{\hat{\varphi}_{R,q}} P(\tau, \hat{\varphi}_{R,q}, \hat{\varphi}_{T,p}) \quad (9)$$

$$\text{ADPS}_{\text{Rx}}(\tau, \hat{\varphi}_{R,q}) = \sum_{\hat{\varphi}_{T,p}} P(\tau, \hat{\varphi}_{R,q}, \hat{\varphi}_{T,p}) \quad (10)$$

In addition to the Fourier-resolution parameter extraction methods, and in order to accurately estimate the location of some reflectors in the channel and compare it to the ground-truth based on the environment, we use a high-resolution parameter extraction (HRPE) method, namely MUSIC (MUltiple Signal Classification) [54]. This algorithm was specifically chosen because of its effectiveness and robustness for accurate DoA and DoD estimations for MPCs in the channel. In quasi-static scenarios where a limited number of MPCs are available, algorithms such as CLEAN or SAGE could as well be used to extract the main MPCs in the channel. However, care needs to be taken when such conditions are not met due to the sampling speed of our prototype; we are sampling at speeds lower than the (Doppler-)Nyquist rate, which indicates that the phase relationships that we normally have as the basis for such HRPE algorithms are not present.

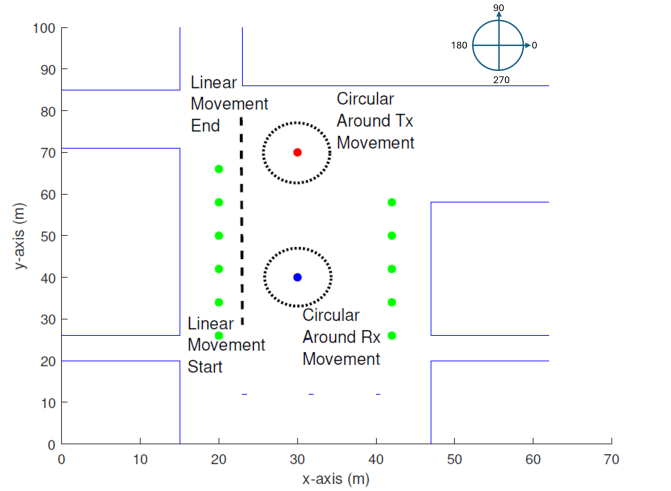


Fig. 12. Reference Measurements Scenarios. Scenario 1 is metallic sphere moving along the linear path from marked start to marked end point. Scenario 2 and 3 are rotation of metallic sphere reflector around Tx and Rx respectively.

V. REFERENCE MEASUREMENTS SCENARIOS

In addition to the calibration measurements performed to verify the functionality of the sounder, we have performed multiple proof-of-concept reference measurements designed to verify the sounder’s ability for dynamic characterization of the channel and the ability to track different reflectors and clusters of MPCs over time. These measurements were done in the same environment as those in Sec. III, but with the addition of artificial reflectors that allowed to determine the ground-truth angles and delays of the associated MPCs from geometric considerations.

A. Dynamic Sphere Reflector Measurements

The first set of these reference measurements used a spherical metallic reflector mounted on top of a tripod and moving along specific tracks as shown in Fig. 12. In the first measurement of that set, the sphere moved on a linear track on one side of the Tx/Rx positions at a speed of 1 m/s. The scenario was measured for 80 seconds, corresponding to a total of 80 MIMO snapshots. The measurement was performed at night to avoid time-variant reflectors (passing-by humans) except for the metallic sphere. The convention that was used for the coordinates system when describing all angles is shown in the compass in Fig. 12, which is adapted throughout the rest of the paper.

Following the process of Sec. IV, we evaluate the omni-PDP, where all delays are multiplied by the speed of light, so that they correspond to distances. We then stack all of these PDPs to visualize the dynamic evolution of PDP vs time, as can be seen in Fig. 13. We can clearly observe the line-of-sight (LoS) component that never changes throughout the measurement, since nothing has obstructed that path during our reference scenario. We also observe the sphere-reflector MPC starting at a delay higher than the LoS delay and coming closer to the LoS as the measurement progresses, reaching a minimum excess delay compared to the LoS when it is

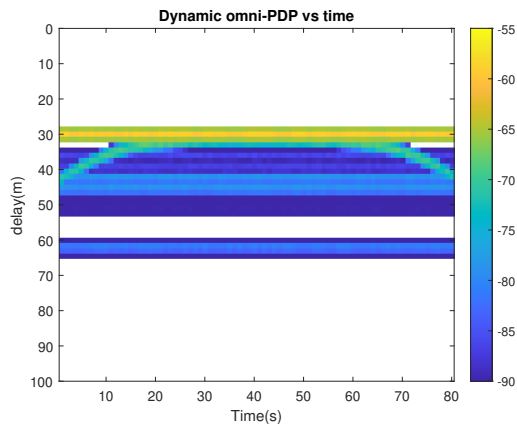


Fig. 13. Dynamic omni-PDP vs time for Linear Sphere movement scenario

at the mid-position between Tx and Rx, after which the delay increases again. We also observe no significant changes in other MPCs seen in the channel, caused by either the surrounding buildings or the trees as shown in Fig. 12.

We also show in Fig. 14 the dynamic evolution of the ADPS for the Tx and the joint Tx-Rx APS. First of all, we notice how each of the MPCs clusters can be dynamically tracked in angle and in delay without ambiguity. We clearly observe the stationary MPCs that remain constant throughout the measurement, and the track followed by the spherical reflector that can be individually seen in the ADPS at the Tx Fig. 14a, and also in the joint APS, Fig. 14b.

In addition to the Fourier-resolution evaluation for this (and subsequent) reference measurements, we also analyze our sounder’s capability in reflector localization and location-tracking across the different MIMO snapshots by localizing the reflector MPCs and accurately estimating their three-dimensional coordinates $(\tau_{\text{ref}}, \phi_{\text{T,ref}}, \phi_{\text{R,ref}})$, where τ_{ref} is estimated from a 10-fold oversampling applied to the omni-PDP (with a corresponding delay resolution of 15 cm), and the angular pair $(\phi_{\text{T,ref}}, \phi_{\text{R,ref}})$ is estimated from the MUSIC spectrum with a 1° angular resolution in both axes. We then compare these coordinates estimates to the ground-truth coordinates of our reflectors as calculated from the measurement geometry.

For the first reference scenario described above, we observe RMSE (root mean square error) of ~ 18 cm in delay, $\sim 10^\circ$ in Tx angle, and $\sim 4^\circ$ in Rx angle. We conjecture that the larger errors in Tx angle are caused by the larger beamwidth of the Tx horn.

The second reference measurement with the sphere reflector consists of moving the reflector in a circular track around the Tx, in order to verify the angular precision of the sounder at the Tx side. The measurement track can also be observed in Fig. 12. The measurement was done with the sphere reflector rotating around the Tx with a rotational speed of $5^\circ/\text{s}$, measuring the full circular track in 72 seconds.

We again visualize the data in terms of dynamic evolution of ADPS at the Tx and dynamic evolution of the joint Tx-Rx APS, in addition to the omni-PDP vs time, as can be seen in Figs. 16 and 15. Starting with the PDP evolution, we see

the main LOS MPC coming at the correct delay (30 m), the reflector starting at an evaluated delay of 34.5 m in comparison to the ground-truth delay of 34.2 m, which is consistent with the accuracy of the previous reference measurement. We also note that it is evolving in a way that is consistent with the trajectory the reflector has taken around the Tx. We also observe how the LOS power drops significantly when the reflector is in a location where it blocks the LOS path. The rest of the MPCs stay constant throughout the duration of the measurement.

As for the angular visualization, we can clearly observe the stationary components throughout the measurement, in addition to no ambiguity in tracking the sphere reflector in its full-circle track around the Tx. As for the high-resolution evaluations with MUSIC, we note RMSE of ~ 14 cm in delay, $\sim 10.5^\circ$ in Tx angle, and $\sim 5^\circ$ in Rx angle, which are again consistent with the accuracies of the previous measurement. We note that while high-resolution methods such as MUSIC provide in general a resolution that exceeds the Fourier resolution of the conventional beamformer, the mean squared error in practical scenarios is bounded by the Cramer-Rao lower bound and depends not only on the SNR, but also the number and strengths of the different MPCs [55].

The third reference measurement with the sphere is similar to the preceding one, but now with the sphere moving in a circle around the Rx, see Fig. 12. We omit discussing the detailed results of this scenario because of similarities with the previous reference scenario. We do note however the RMSE results of ~ 14.5 cm in delay, $\sim 10^\circ$ in Tx angle, and $\sim 4.8^\circ$ in Rx angle, which are again within our sounder’s accuracy estimates.

B. Moving Rx Measurement

In addition to the previously measured reference scenarios, we have measured a dynamic scenario where the Tx and Rx were mounted on carts (about 1.5 m above ground), and performed a measurement that mimics a car-to-car environment where one car is driving away from the other one. A diagram representation of the measurement environment is shown in Fig. 17. The Tx stays stationary throughout the measurement, while the Rx starts moving from a 4 m distance with respect to the Tx at a speed of 1 m/s until it stops at 56 m away from the Tx. The LoS path is maintained throughout the measurement, while other propagation paths may vary depending on surrounding objects.

We again visualize the results in terms of dynamic evolution of omni-PDP and the dynamic ADPSs at both Tx and Rx, see Figs. 19 and 18. The un-obstructed LoS path is present throughout the measurement, with increasing delay corresponding to the increasing displacement of the Rx cart. The wall reflection MPCs start at a wide angle compared to the LoS path; $(\phi_{\text{T}}, \phi_{\text{R}}) = (45^\circ, -45^\circ)$ for reflection on building B, and $(\phi_{\text{T}}, \phi_{\text{R}}) = (168^\circ, -168^\circ)$ for reflection on building C. These MPCs then get closer to the LoS path in both angle and delay as the Rx gets further away from the Tx, which conforms again with the geometry of the scenario. At the final position (when the Rx is 56 m away

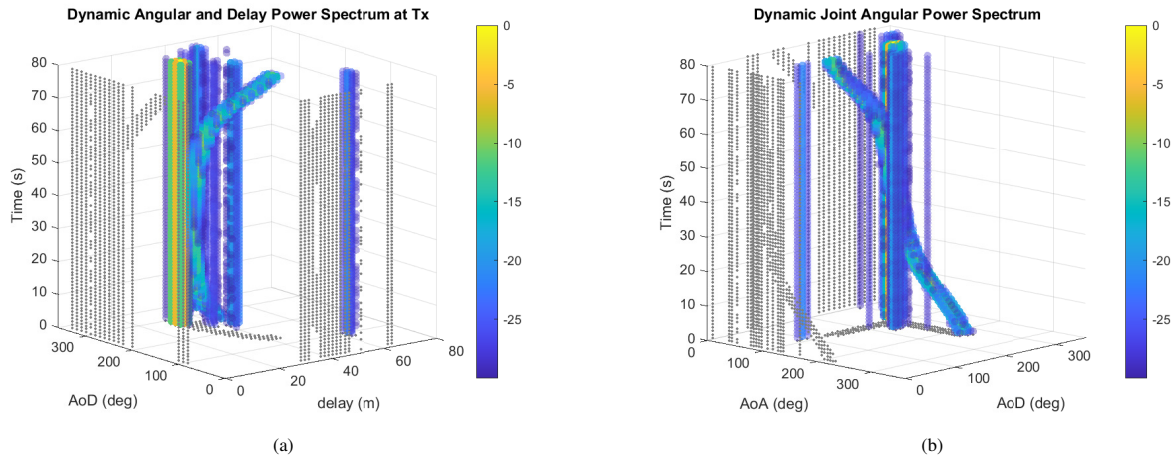


Fig. 14. Dynamic evaluation in the linear sphere movement scenario, (a) ADPS at Tx, (b) joint APS. Shown in grey are the projections on each of the dimensions (marginal data).

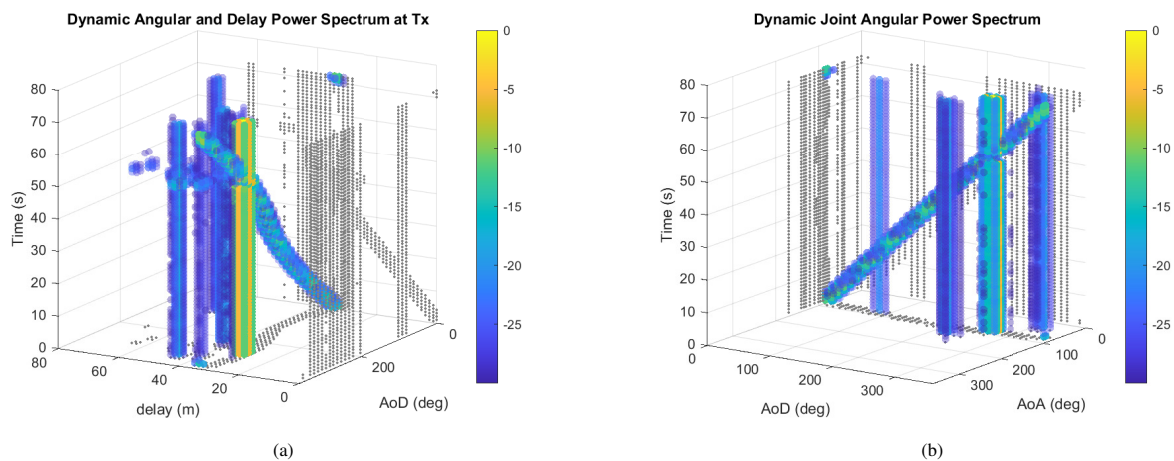


Fig. 15. Dynamic evaluation in the circular sphere around Tx movement scenario, (a) ADPS at Tx, (b) joint APS. Shown in grey are the projections on each of the dimensions (marginal data).

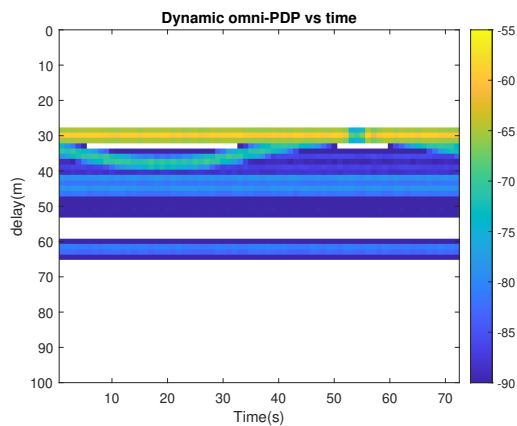


Fig. 16. Dynamic omni-PDP vs time for Circular Sphere around Tx movement scenario

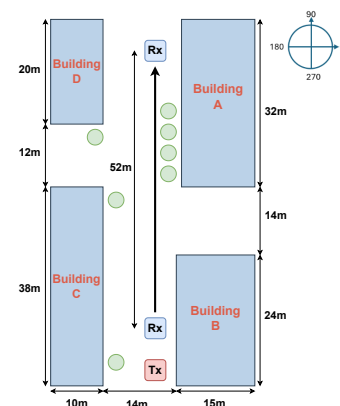


Fig. 17. Moving Rx measurement scenario

from the Tx), we observe the reflection from building C still present at $(\phi_T, \phi_R) = (110^\circ, -110^\circ)$, while the MPC reflected

on building B has disappeared. We observe the birth of an additional double-reflection MPC reflected on building C then A before reaching the receiver. We also observe many MPCs

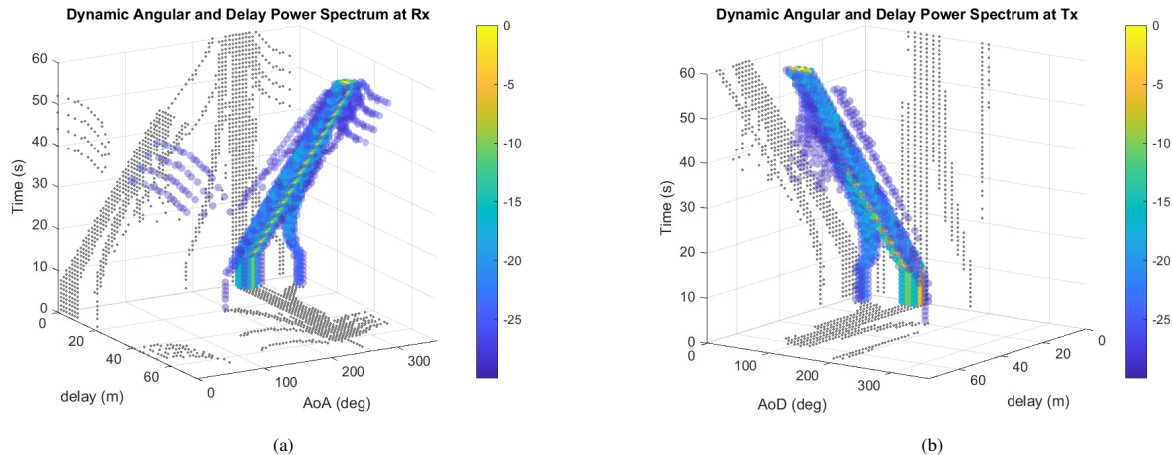


Fig. 18. Dynamic evaluation in the Moving Rx away from Tx scenario, (a) ADPS at Rx, (b) ADPS at Tx. Shown in grey are the projections on each of the dimensions (marginal data). Reflection from building B can be identified in (b) as the component starting at around (delay, AoD) = (9, 45), while building C can be identified in (b) as the component starting at around (delay, AoD) = (20, 160) and can be tracked afterwards.

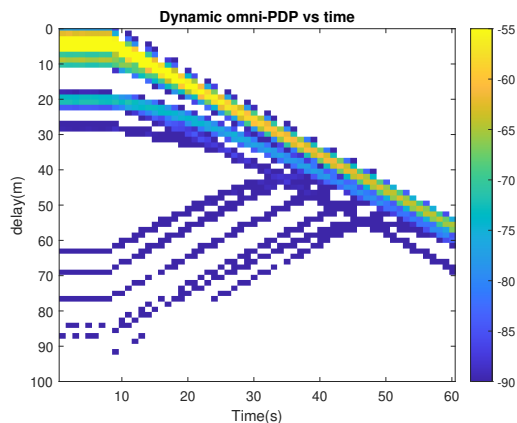


Fig. 19. Dynamic omni-PDP vs time for Rx Moving Away from Tx scenario

that are present throughout the measurement which were traced to be originated as diffractions caused by cylindrical lampposts and trees in the measurement environment. An additional scenario (T-intersection with intermittent LOS) is presented and analyzed in our conference paper [1].

VI. CONCLUSION

This paper introduced a new concept for channel sounding, called ReRoMA, which retains the simplicity, low cost and flexibility of rotating-horn channel sounders while drastically improving measurement speed. Our prototype enables scanning of the full 360° range in azimuth at both Tx and Rx, allowing the capture of a MIMO snapshot with 36×72 orientation combinations within the stationarity time of a dynamic channel. A series of reference measurements with a defined-location spherical reflector verified the angular and delay accuracy of our sounder, showing delay accuracy of 17 cm, and angular accuracy at Tx and Rx of 10 and 4.5 degree, respectively. Moreover, we have performed a proof-of-concept measurement of a dynamic cart-to-cart scenario at 60 GHz mimicking a car moving away from another, and

shown the ability of the sounder to directionally resolve and track the different propagation paths in angle and delay. Some calibration and reference sample measurements using this sounder will be made publicly available on the WiDeS website.

The ReRoMA concept is flexible and can be extended in a variety of ways. Firstly, adjustment to other frequency bands is easily possible. Similarly, increased measurement bandwidth just requires change of the baseband signal generation/capture and RF filter bandwidth. Different tradeoffs between measurement speed and Tx beamwidth can lead to higher angular resolution. Finally, fully polarimetric measurements can be achieved by using a (high-power) polarization switch at the Tx as well. All this will be subject of our future work.

VII. ACKNOWLEDGMENTS

We would like to thank the METRANS project, and in particular Genevieve Giuliano, Cort Brinkerhoff and Katrina Soriano for their kind help in handling many administrative issues over the duration of the project. We would like to also thank the WiDeS@USC group members, especially Guillermo Castro and Jorge Gomez-Ponce, for their help in the hardware design and measurement campaign.

REFERENCES

- [1] H. Hammoud *et al.*, "A novel low-cost channel sounder for double-directionally resolved measurements in the mmwave band," *IEEE International Conference on Communications*, p. under review, 2024.
- [2] A. F. Molisch, *Wireless Communications: From Fundamentals to Beyond 5G*, 3rd ed. IEEE Press - Wiley, 2023.
- [3] A. F. Molisch *et al.*, "Spinning directional antenna in centimeter and millimeter wave bands," Patent WO 2022155493 A1, sep 2022, available at: <https://patents.google.com/patent/WO2022155493A1/en>.
- [4] P. F. Smulders *et al.*, "Frequency-domain measurement of the millimeter wave indoor radio channel," *IEEE Transactions on Instrumentation and Measurement*, vol. 44, no. 6, pp. 1017–1022, 1995.
- [5] J. Lee *et al.*, "Omnidirectional millimeter-wave propagation characteristics of corridor environments based on measurements at 28, 38, 71 and 82 GHz," in *2022 16th European Conference on Antennas and Propagation (EuCAP)*, 2022, pp. 1–5.

- [6] G. Lovnes *et al.*, "Channel sounding measurements at 59 GHz in city streets," in *5th IEEE International Symposium on Personal, Indoor and Mobile Radio Communications, Wireless Networks-Catching the Mobile Future.*, vol. 2. IEEE, 1994, pp. 496–500.
- [7] H. Xu *et al.*, "Measurements and models for 38-GHz point-to-multipoint radiowave propagation," *IEEE Journal on Selected Areas in Communications*, vol. 18, no. 3, pp. 310–321, 2000.
- [8] E. Zöchmann *et al.*, "Position-specific statistics of 60 GHz vehicular channels during overtaking," *IEEE Access*, vol. 7, pp. 14 216–14 232, 2019.
- [9] J. Hejlselbaek *et al.*, "Channel sounding system for mm-wave bands and characterization of indoor propagation at 28 GHz," *International journal of wireless information networks*, vol. 24, no. 3, pp. 204–216, 2017.
- [10] Z. Wen *et al.*, "mmWave MIMO channel sounding for 5G," in *1st International Conference on 5G for Ubiquitous Connectivity*. IEEE, 2014, pp. 192–197.
- [11] X. Cai *et al.*, "A switched array sounder for dynamic millimeter-wave channel characterization: Design, implementation and measurements," *IEEE Transactions on Antennas and Propagation*, 2023, early access.
- [12] H. Tataria *et al.*, "27.5-29.5 GHz switched array sounder for dynamic channel characterization: Design, implementation and measurements," *arXiv preprint arXiv:2105.10712*, 2021.
- [13] R. Sun *et al.*, "Design and calibration of a double-directional 60 GHz channel sounder for multipath component tracking," in *2017 11th European Conference on Antennas and Propagation (EUCAP)*, 2017, pp. 3336–3340.
- [14] J. O. Nielsen *et al.*, "A channel sounder for massive MIMO and mmWave channels," *IEEE Communications Magazine*, vol. 56, no. 12, pp. 67–73, 2018.
- [15] C. U. Bas *et al.*, "A real-time millimeter-wave phased array MIMO channel sounder," in *2017 IEEE 86th Vehicular Technology Conference (VTC-Fall)*. IEEE, 2017, pp. 1–6.
- [16] —, "Real-time millimeter-wave mimo channel sounder for dynamic directional measurements," *IEEE Transactions on Vehicular Technology*, vol. 68, no. 9, pp. 8775–8789, 2019.
- [17] C. Slezak *et al.*, "Empirical effects of dynamic human-body blockage in 60 GHz communications," *IEEE Communications Magazine*, vol. 56, no. 12, pp. 60–66, 2018.
- [18] D. Caudill *et al.*, "Omnidirectional channel sounder with phased-array antennas for 5G mobile communications," *IEEE Transactions on Microwave Theory and Techniques*, vol. 67, no. 7, pp. 2936–2945, 2019.
- [19] —, "Real-Time mmWave Channel Sounding Through Switched Beamforming With 3-D Dual-Polarized Phased-Array Antennas," *IEEE Transactions on Microwave Theory and Techniques*, vol. 69, no. 11, pp. 5021–5032, 2021.
- [20] A. Chopra *et al.*, "Real-time millimeter wave omnidirectional channel sounder using phased array antennas," in *GLOBECOM 2020-2020 IEEE Global Communications Conference*. IEEE, 2020, pp. 1–7.
- [21] —, "A real-time millimeter wave V2V channel sounder," in *2022 IEEE Wireless Communications and Networking Conference (WCNC)*. IEEE, 2022, pp. 2607–2612.
- [22] C. Gustafson *et al.*, "On mm-wave multipath clustering and channel modeling," *IEEE Transactions on Antennas and Propagation*, vol. 62, no. 3, pp. 1445–1455, 2013.
- [23] J. Huang *et al.*, "Multi-frequency mmwave massive MIMO channel measurements and characterization for 5G wireless communication systems," *IEEE Journal on Selected Areas in Communications*, vol. 35, no. 7, pp. 1591–1605, 2017.
- [24] Q. Guo *et al.*, "Measurement of millimeter-wave 3D MIMO channel in large indoor environment," in *2021 15th European Conference on Antennas and Propagation (EuCAP)*. IEEE, 2021, pp. 1–5.
- [25] H.-A. Nguyen *et al.*, "Instantaneous direction of arrival measurements in mobile radio channels using virtual circular array antennas," in *2016 IEEE Globecom Workshops (GC Wkshps)*. IEEE, 2016, pp. 1–7.
- [26] K. Haneda *et al.*, "A statistical spatio-temporal radio channel model for large indoor environments at 60 and 70 GHz," *IEEE Transactions on Antennas and Propagation*, vol. 63, no. 6, pp. 2694–2704, 2015.
- [27] A. W. Mbugua *et al.*, "Millimeter wave multi-user performance evaluation based on measured channels with virtual antenna array channel sounder," *Ieee Access*, vol. 6, pp. 12 318–12 326, 2018.
- [28] S. L. Nguyen *et al.*, "Comparing radio propagation channels between 28 and 140 GHz bands in a shopping mall," pp. 1–5, 2018.
- [29] T. S. Rappaport *et al.*, "Millimeter wave mobile communications for 5G cellular: It will work!" *IEEE Access*, vol. 1, pp. 335–349, 2013.
- [30] Y. Xing *et al.*, "Propagation measurements and path loss models for sub-THz in urban microcells," 2021.
- [31] G. R. MacCartney *et al.*, "A flexible millimeter-wave channel sounder with absolute timing," *IEEE Journal on Selected Areas in Communications*, vol. 35, no. 6, pp. 1402–1418, 2017.
- [32] S. Hur *et al.*, "Synchronous channel sounder using horn antenna and indoor measurements on 28 GHz," in *2014 IEEE International Black Sea Conference on Communications and Networking (BlackSeaCom)*. IEEE, 2014, pp. 83–87.
- [33] M.-D. Kim *et al.*, "Directional delay spread characteristics based on indoor channel measurements at 28 GHz," in *2015 IEEE 26th Annual International Symposium on Personal, Indoor, and Mobile Radio Communications (PIMRC)*. IEEE, 2015, pp. 403–407.
- [34] D. Dupleich *et al.*, "Multi-Band Propagation and Radio Channel Characterization in Street Canyon Scenarios for 5G and Beyond," *IEEE Access*, vol. 7, pp. 160 385–160 396, 2019.
- [35] A. Maltsev *et al.*, "Experimental investigations of 60 GHz WLAN systems in office environment," *IEEE Journal on Selected Areas in Communications*, vol. 27, no. 8, pp. 1488–1499, 2009.
- [36] F. Erden *et al.*, "28 GHz mmwave channel measurements and modeling in a library environment," in *2020 IEEE Radio and Wireless Symposium (RWS)*, 2020, pp. 52–55.
- [37] S. Nie *et al.*, "72 GHz millimeter wave indoor measurements for wireless and backhaul communications," in *2013 IEEE 24th Annual International Symposium on Personal, Indoor, and Mobile Radio Communications (PIMRC)*. IEEE, 2013, pp. 2429–2433.
- [38] N. A. Abbasi *et al.*, "THz band channel measurements and statistical modeling for urban microcellular environments," *IEEE Transactions on Wireless Communications*, 2023, early access.
- [39] —, "THz band channel measurements and statistical modeling for urban d2d environments," *IEEE T. Wireless Comm.*, pp. 1466–1479, 2022.
- [40] T. Doeker *et al.*, "Channel measurements and modeling for low terahertz communications in an aircraft cabin," *IEEE Transactions on Antennas and Propagation*, vol. 70, no. 11, pp. 10903–10916, 2022.
- [41] P. Zhang *et al.*, "Indoor small-scale spatiotemporal propagation characteristics at multiple millimeter-wave bands," *IEEE Antennas and Wireless Propagation Letters*, vol. 17, no. 12, pp. 2250–2254, 2018.
- [42] B. De Beelde *et al.*, "V-band channel modeling, throughput measurements, and coverage prediction for indoor residential environments," *Electronics*, vol. 11, no. 4, p. 659, 2022.
- [43] T. S. Rappaport *et al.*, "38 GHz and 60 GHz angle-dependent propagation for cellular & peer-to-peer wireless communications," in *2012 IEEE International Conference on Communications (ICC)*. IEEE, 2012, pp. 4568–4573.
- [44] P. Zhang *et al.*, "Millimeter-wave space-time propagation characteristics in urban macrocell scenarios," in *ICC 2019-2019 IEEE International Conference on Communications (ICC)*. IEEE, 2019, pp. 1–6.
- [45] J. Du *et al.*, "Directional measurements in urban street canyons from macro rooftop sites at 28 GHz for 90% outdoor coverage," *IEEE Transactions on Antennas and Propagation*, vol. 69, no. 6, pp. 3459–3469, 2021.
- [46] C. A. Fernandes *et al.*, "Review of 20 years of research on microwave and millimeter-wave lenses at" instituto de telecomunicações," *IEEE Antennas and Propagation Magazine*, vol. 57, no. 1, pp. 249–268, 2015.
- [47] N. Ntetsikas *et al.*, "60 GHz Outdoor to Indoor (O2I) propagation measurements in a university campus," in *2022 IEEE 23rd International Workshop on Signal Processing Advances in Wireless Communication (SPAWC)*. IEEE, 2022, pp. 1–5.
- [48] H. Groll *et al.*, "Scanning aperture antennas with spherical shells," in *2019 International Conference on Electromagnetics in Advanced Applications (ICEAA)*. IEEE, 2019, pp. 1220–1223.
- [49] L. Bernadó *et al.*, "The (in-) validity of the wssus assumption in vehicular radio channels," in *2012 IEEE 23rd International Symposium on Personal, Indoor and Mobile Radio Communications-(PIMRC)*. IEEE, 2012, pp. 1757–1762.
- [50] Millimeter Wave Products Inc., "Waveguide polarization switch: Frequency 50 GHz - 75 GHz, cross polarization -20 db, 90 degrees or rh/lh polarization, 30 ma," Millimeter Wave Products Inc., 2023, accessed: 2023-11-08. [Online]. Available: <https://www.miwv.com/waveguide-polarization-switch-frequency-50-ghz-75-ghz/>
- [51] R. Wang *et al.*, "A real-time mimo channel sounder for vehicle-to-vehicle propagation channel at 5.9 GHz," in *2017 IEEE International Conference on Communications (ICC)*. IEEE, 2017.
- [52] A. F. Molisch *et al.*, "Measurement of the capacity of mimo systems in frequency-selective channels," in *IEEE VTS 53rd Vehicular Technology Conference, Spring 2001. Proceedings (Cat. No. 01CH37202)*, vol. 1. IEEE, 2001, pp. 1–6.

- [53] J. Gomez-Ponce *et al.*, “Impact of noisy measurements with fourier-based evaluation on condensed channel parameters,” *IEEE Transactions on Wireless Communications*, 2023.
- [54] R. Schmidt, “Multiple emitter location and signal parameter estimation,” *IEEE Transactions on Antennas and Propagation*, vol. 34, no. 3, pp. 1–5, 1986.
- [55] B. H. Fleury, M. Tschudin, R. Heddergott, D. Dahlhaus, and K. I. Pedersen, “Channel parameter estimation in mobile radio environments using the sage algorithm,” *IEEE Journal on selected areas in communications*, vol. 17, no. 3, pp. 434–450, 1999.